Welding in the World (2020) 64:1437–1448
https://doi.org/10.1007/s40194-020-00955-7

RESEARCH PAPER

Modeling the influence of injection parameters on powder efficiency in laser cladding

Xinyong Gong[1] · Wei You[1] · Xu Li[2] · Lei Wang[1]

Received: 11 October 2019 / Accepted: 2 July 2020 / Published online: 12 July 2020

Abstract

For lateral powder injection, adjustments of defocusing distance, powder feeding angle, and molten pool width are set as input variables, and the powder transport vector, powder outflow position vector, and the injection offset vector are determined. The powder transport model involving above adjustment parameters is constructed based on operation of such vectors, which have been verified in experiments. Then, powder transport ratios of three variables with 13 × 13 × 5 levels are calculated to reflect the effect of injection parameters, which increases with the molten pool width, and maintains a high level as the defocusing distance and powder feeding angle are both adjusted positively (clockwise) or negatively (anti-clockwise). In addition, the powder transport ratio corresponding to an arbitrary combination of injection parameters can be calculated and its process window could be extended to determine a better process combination.

Keywords Laser cladding · Powder transport model · Vector operation · Injection parameters · Process window

Nomenclature

Input variables of the model

χ	[mm] Adjustment of defocusing distance
α	[°] Adjustment of powder feeding angle
δ	[mm] Adjustment of molten pool width

Initial condition variables

D	[mm] Laser beam diameter
g	[m/s^2] Gravity acceleration
W	[mm] Distance from nozzle to laser beam center in x direction
L	[mm] Distance from nozzle to laser beam center in z direction
V_{P0}	[mm/s] Initial velocity of powders from nozzle
φ	[°] Divergence angle of powder flux (Fig. 1)
θ	[°] The angle from axis of powder nozzle to horizontal
V_m	[g/min] Powder feed rate
V_s	[mm/s] Velocity of laser beam

Other model variables

ξ	Mass ratio of measured cladding layer to all powder injected from the powder feeding nozzle
ξ_{PT}	Mass ratio of powder fed into the molten pool to all powder injected from the powder feeding nozzle
V_{PE}	[mm/s] Terminal velocity of powder particles
V_t	[mm/s] Component of terminal velocity in Z-axis direction for powder particles
$m(z_1)$	[g] Mass of powder particles stored in space with dz_1 distance in Z_1 direction
t_{dz1}	[s] Time for particle to move dz_1 distance
$C_G(z_1)$	[g/mm] Particle mass distribution of Gaussian powder flux per unit length in Z_1 direction
$C_G^{\alpha}(x_1,z_1)$	[g/mm^2] Concentration distribution for Gaussian flux in S_1 coordinate system after adjustment of defocusing distance and powder feeding angle
ξ_{PT}^{G}	Transport ratio of powder flow field with Gaussian distribution

Recommended for publication by Commission I - Additive Manufacturing, Surfacing, and Thermal Cutting

✉ Xinyong Gong
huagu1984@126.com

[1] School of Mechanical and Electrical Engineering, North China Institute of Science and Technology, No.467 Xueyuan Street, Langfang 065201, People's Republic of China

[2] Hebei Key Laboratory of Safety Monitoring of Mining Equipment, North China Institute of Science and Technology, No.467 Xueyuan Street, Langfang 065201, People's Republic of China

μ	Mathematical expectation (mean) of Gaussian distribution
σ	Standard deviation of Gaussian distribution
$x(P_1)$, $x(P_2)$	X coordinate of powder flux boundary in S (XOZ) coordinate system (Fig. 1)
$x(P_3)$, $x(P_4)$	X coordinate of powder flux boundary falling into the molten pool in S (XOZ) coordinate system (Fig. 1)
$x(Q_1)$, $x(Q_2)$	X_1 coordinate of powder flux boundary in $S_1(X_1OZ_1)$ coordinate system (Fig. 1)
$x(Q_3)$, $x(Q_4)$	X_1 coordinate of powder flux boundary falling into the molten pool in $S_1(X_1OZ_1)$ coordinate system (Fig. 1)
A, A_1, A_2	Outflow position of powder from nozzle with initial condition/defocus distance adjustment/powder feeding angle adjustment
O, M, N	Injection position of central particle with initial condition/defocus distance adjustment/powder feeding angle adjustment
$\overrightarrow{AO}$, $\overrightarrow{A_1M}$, $\overrightarrow{A_2N}$	Powder transport vector from outflow position (A, A_1, A_2) to injection position (O, M, N)
L_{AO}, L^{X}_{AO}, L^{α}_{AO}	[mm] Length of powder transport vector $\overrightarrow{AO}$, $\overrightarrow{A_1M}$, $\overrightarrow{A_2N}$
γ, γ_1, γ_2	[°] Inclination angle of powder transport vector $\overrightarrow{AO}$, $\overrightarrow{A_1M}$, $\overrightarrow{A_2N}$
L_{AO},	[mm] Length of lateral feeding tube from fulcrum to outflow position
$\overrightarrow{OA_1}$, $\overrightarrow{OA_2}$	Outflow position vector from coordinate origin O to outflow position after adjustment of defocus distance/powder feeding angle
$x(\overrightarrow{OA_2})$, $z(\overrightarrow{OA_2})$	Coordinates in X, Z directions of outflow position A_2 (Fig. 3(b))
$\overrightarrow{OM}$, $\overrightarrow{ON}$	Injection offset vector from coordinate origin O to injection position after adjustment of defocus distance/powder feeding angle
i, j	unit vector in X, Z directions (Fig. 3)
x_1, x_2	X coordinate of vector $\overrightarrow{OM}$, $\overrightarrow{MN}$
O'	Initial fulcrum position of powder feeding nozzle
O'_1	Fulcrum position after defocus distance adjustment
$\overrightarrow{O'_1A_1}$, $\overrightarrow{O'_1A_2}$	Vector from fulcrum position to outflow position after adjustment of defocus distance/powder feeding angle
$\gamma_{\overrightarrow{MA_2}}$	[°] Angle of vector $\overrightarrow{MA_2}$ to the horizontal (Fig. 3)
S, S_N	Coordinate system with injection position of point O, N as origin (Fig. 3)
x_α, z_α	x, z-coordinate in S_N coordinate system (Fig. 3(b))

1 Introduction

Laser cladding [1] is an application technology which involves laser, gas, powder, flow of molten metal, heat conduction, radiation, convection, etc. Complex coupling mechanisms exist among these factors [2]. Many process parameters of laser cladding can affect or determine morphology of the cladding layer, such as laser energy distribution [3], laser scanning speed [4], powder nozzle shape, and powder injection conditions [5]. The study of these interaction mechanisms and the effect of process parameters are very important to control precisely the mass/size of cladding layer [6, 7].

The cross-sectional area of a single cladding layer is determined by powder feeding rate (V_m), powder utilization efficiency (ξ), and laser travel speed (V_S) [8]. Generally, in order to achieve metallurgical bonding of the cladding layer or reduce residual stress and deformation of deposition parts, the main process parameters such as V_m and V_S can be adjusted only in a small range. Thus, ξ becomes a key factor to control the mass/size of cladding layer. Currently, few researches have been done on the influence of process parameters on ξ. Through a catchment model, Lin [9] investigated powder catchment efficiency in the process of coaxial powder feeding. With increasing of defocusing distance and powder feeding angle, and decreasing of the ratio (beam spot diameter/powder impact diameter), the powder efficiency declined gradually. Andrew [10] studied the laser deposition efficiency of multiple-layer thin-wall parts. The standoff distance between powder nozzle and material deposition point was set as a variable factor in his experiment. Compared with variable-step and no-step method, poorer results were obtained by fixed-step laser scanning mode, in which the standoff distance increased a constant amount per layer. The highest powder efficiency was gained with the "no-step" method. Liu [11, 12] suggested that powder primary efficiency was dependent on an exponential function involving the ratio of melt pool width to powder flow diameter.

Powder transport ratio (ξ_{PT}), namely the mass ratio of powder particles fed into the molten pool to all powders ejected from the powder feeding nozzle, depends on particle concentration distribution and boundaries of powder flux [8, 13]. For laser cladding by lateral powder feeding, the powder nozzle is fixed on one side of the laser head by a powder feeding tube usually. Above boundary condition is mainly controlled by nozzle position(/inclination angle) and molten pool width, the former of which is changed with adjustment of defocusing distance and powder feeding angle, and the latter with laser power, scanning speed, and powder feed rate. Because of the similarity of the two physical parameters ξ and ξ_{PT}, analytical

solutions of ξ_{PT} involving adjustments of injection parameters such as defocusing distance, powder feeding angle, and molten pool width are deduced and their effects on ξ_{PT} are discussed in this article taking the size/mass control of cladding layer as research purpose.

2 Analytical model

2.1 Influential factors

Based on the modeling process of powder transport model established in [8, 13], some features can be listed as follows. As shown in Fig. 1, powder particles from point A move obliquely downward under gravity but in different initial velocity direction (θ–φ~θ+φ), and their flight trajectories conform to the kinematics equation. Particles at the edge/center of divergence angle would fall on point P_1, P_2/O. Parabolic trajectory ($\widehat{AP_1}, \widehat{AP_2}, \widehat{AO}$) for particles was simplified as a straight line trajectory, which would not affect the estimation of ξ_{PT} in the initial model. Boundaries (AP_1, AP_2) of the powder flux are determined by the outflow position ($-W$, L) of the central particles, inclination angle of powder feeding nozzle (θ), and divergence angle of powder flux (φ) (Eqs. (4, 5, 8) in [13]). Boundaries (AP_3, AP_4) of powders falling into the molten pool are codetermined by the outflow position ($-W$, L) and molten pool boundary (Eqs. (6–8) in [13]). The particle concentration distribution is calculated by linear trajectory of center particles moving from the outflow position A to the injection position O, which can be characterized by the distance (L_{AO}) and inclination angle (γ) between above two points (Eq. (20) in [13] and Eq. (3) in [8]).

In this model, the outflow and injection positions of central particles are changed with adjustments of defocusing distance and powder feeding angle, and the molten pool boundary moves with variation of the pool width. The new coordinate position information can be re-substituted into the original theoretical model to calculate the powder transport ratio after adjustment of injection parameters.

- The effect of defocusing distance adjustment on the physical model is presented in Fig. 2(a). The adjustment amount is χ and the movement of the powder nozzle away from the workpiece is taken as positive. By $+\chi$ adjustment, therefore, the height of the outflow position and the range of powder flow boundaries (P_1, P_2) increase, and the injection position of the central particles moves in $+X$ direction. The situation is reverse for $-\chi$ adjustment. A parallel laser beam is assumed, so the width of the molten pool would not be changed with the adjustment.
- The effect of the powder feeding angle adjustment on the physical model is presented in Fig. 2(b). As the nozzle orifice position is fixed, the outflow position is changed by the rotation around the fixed point of tube (fulcrum). The adjustment amount is α and rotation of powder nozzle in clockwise direction is taken as positive. By $+\alpha$ adjustment, injection position and powder flow boundaries (P_1, P_2) move toward $-X$ direction. The situation is reverse by $-\alpha$ adjustment. Here we assume that the molten pool width would not be changed with the variation of particle concentration distribution caused by this adjustment.
- The effect of molten pool width adjustment on the physical model is presented in Fig. 2(c). The adjustment

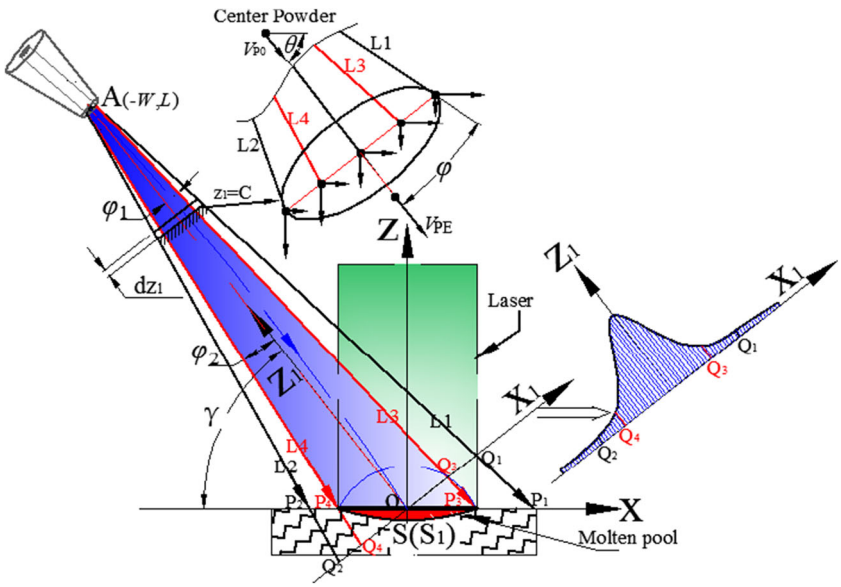

Fig. 1 Physical model for initial Gaussian powder flow field

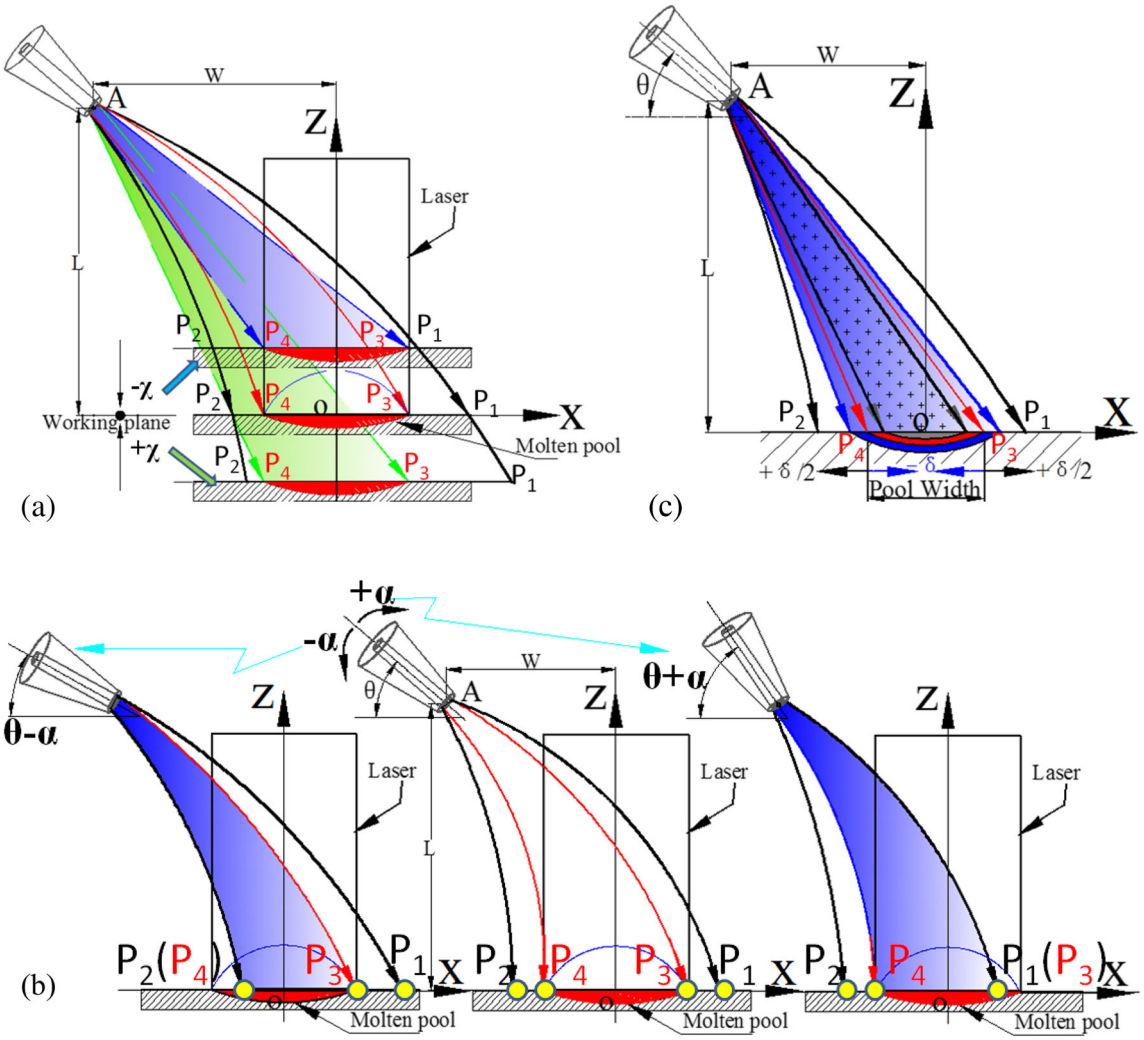

Fig. 2 Physical model for each parameter adjustment. (a) Defocusing distance adjustment. (b) Powder feeding angle adjustment. (c) Pool width adjustment

amount is δ. Boundaries (P_3, P_4) of powders falling into the pool are moved by this adjustment, and the powder transport ratio is changed.

2.2 Model derivation

In order to make these three adjustments unified into one mathematical model, the sequence of the derivation process is defocusing distance $+\chi$, powder feeding angle $+\alpha$, and pool width $-\delta$. Based on the model analysis above, the key of modeling is information on outflow position, injection position, and pool boundary. The trajectory of the central particle from the outflow to injection position is related with $+\chi$ and $+\alpha$ adjustments, which are hard to determine. This article attempts to obtain the information using vector computing method. Among the vectors shown in Fig. 3, the powder transport vector is defined by vectors $\overrightarrow{AO}$ $\left(\overrightarrow{A_1M},\ \overrightarrow{A_2N}\right)$ from the central particles outflow position A (A_1, A_2) to injection position O, M, N. The outflow position vector is defined by vectors $\overrightarrow{OA_1}$ $\left(\overrightarrow{OA_2}\right)$ from coordinate origin O to outflow position A_1, A_2. Injection offset vector is defined by vectors $\overrightarrow{OM}, \overrightarrow{ON}$ from coordinate origin O to injection position M, N. The outflow and injection position can be obtained by solving the vectors mentioned above.

2.2.1 Adjustment of defocusing distance

The geometric relationship among vectors of pre and post adjustment is shown in Fig. 3(a). The initial outflow position is known as point A $(-W, L)$. After $+\chi$ adjustment, the outflow position vector can be determined by Eq. (1).

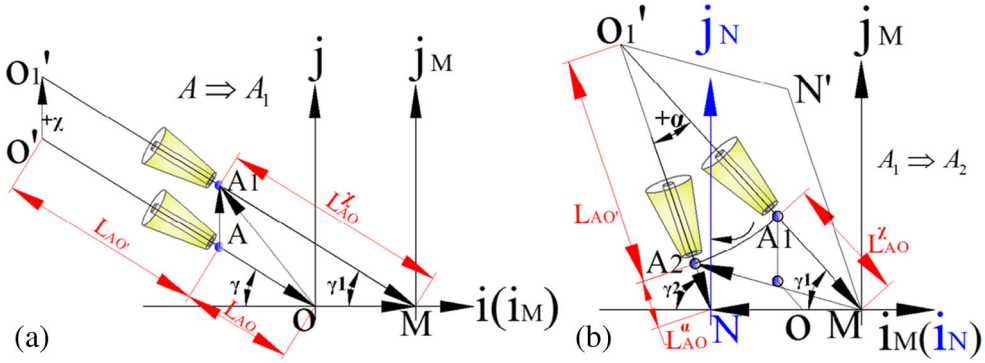

Fig. 3 Geometric relationship of related vector. (a) Defocusing distance adjustment. (b) Powder feeding angle adjustment

$$\overrightarrow{OA_1} = \overrightarrow{AA_1} - \overrightarrow{AO} = \chi \cdot j - W \cdot i + L \cdot j = -W \cdot i + (L + \chi) \cdot j \quad (1)$$

Powder transport vector is changed from $\overrightarrow{AO}$ to $\overrightarrow{A_1M}$. The length of this vector is increased but the inclination is constant,

$$\gamma_1 = \gamma \quad (2)$$

If we suppose,

$$\overrightarrow{OM} = x_1 i \quad (3)$$

Then,

$$\overrightarrow{A_1M} = \overrightarrow{OM} - \overrightarrow{OA_1} = (x_1 + W)i - (L + \chi)j \quad (4)$$

By relationship of vector expression and its inclination

$$\tan\gamma_1 = \left|\frac{-(L+\chi)}{x_1 + W}\right| \quad (5)$$

We can conclude as follows:

$$x_1 = \frac{L+\chi}{\tan\gamma} - W \quad (6)$$

Then, the injection offset vector and powder transport vector are determined. In addition, the transport length of the central particles is changed to

$$L_{AO}^{\chi} = \left|\overrightarrow{A_1M}\right| \quad (7)$$

2.2.2 Adjustment of powder feeding angle

The geometric relationship among the vectors of pre and post adjustment is shown in Fig. 3(b). Rotation around $O_1^{'}$ from vector $\overrightarrow{O_1^{'}A_1}$ to vector $\overrightarrow{O_1^{'}A_2}$ characterizes movement of powder feeding tube. Outflow position moves from A_1 to A_2. Powder transport vector and its inclination are changed from $\overrightarrow{A_1M}$ (γ_1) to $\overrightarrow{A_2N}$ (γ_2). By geometric relationships in $\triangle O_1^{'}MN$,

$$\gamma_2 = \gamma_1 + \alpha \quad (8)$$

So we can conclude that

$$\overrightarrow{MA_2} = \overrightarrow{N'O_1'} = \overrightarrow{MO_1'} - \overrightarrow{MN'} \quad (9)$$

$$\overrightarrow{MO_1'} = -\left(L_{AO}^{\chi} + L_{AO'}\right)\cos\gamma \cdot i + \left(L_{AO}^{\chi} + L_{AO'}\right)\sin\gamma \cdot j \quad (10)$$

$$\overrightarrow{MN'} = -L_{AO'}\cos(\gamma+\alpha) \cdot i + L_{AO'}\sin(\gamma+\alpha) \cdot j \quad (11)$$

By Eqs. (9–11), length, inclination, and mathematical expression of vector $\overrightarrow{MA_2}$ can be determined in Eqs. (12–14).

$$\left|\overrightarrow{MA_2}\right| = \sqrt{\left[\left(L_{AO}^{\chi} + L_{AO'}\right)\cos\gamma - L_{AO'}\cos(\gamma+\alpha)\right]^2 + \left[\left(L_{AO}^{\chi} + L_{AO'}\right)\sin\gamma - L_{AO'}\sin(\gamma+\alpha)\right]^2} \quad (12)$$

$$\gamma_{\overrightarrow{MA2}} = \arctan\left|\frac{-\left(L_{AO}^{\chi} + L_{AO'}\right)\sin\gamma + L_{AO'}\sin(\gamma+\alpha)}{\left(L_{AO}^{\chi} + L_{AO'}\right)\cos\gamma - L_{AO'}\cos(\gamma+\alpha)}\right| \quad (13)$$

$$\overrightarrow{MA_2} = -\left|\overrightarrow{MA_2}\right| \cdot \cos\gamma_{\overrightarrow{MA2}} \cdot i + \left|\overrightarrow{MA_2}\right| \cdot \sin\gamma_{\overrightarrow{MA2}} \cdot j \quad (14)$$

If we suppose,

$$\overrightarrow{MN} = -x_2 i \quad (15)$$

Then,

$$\overrightarrow{A_2N} = \overrightarrow{MN} - \overrightarrow{MA_2} = \left(-x_2 + \left|\overrightarrow{MA_2}\right| \cdot \cos\gamma_{\overrightarrow{MA2}}\right) \cdot i - \left|\overrightarrow{MA_2}\right| \cdot \sin\gamma_{\overrightarrow{MA2}} \cdot j \tag{16}$$

By the relationship of the vector expression and its inclination,

$$\tan\gamma_2 = \left| \frac{\left|\overrightarrow{MA_2}\right| \cdot \sin\gamma_{\overrightarrow{MA2}}}{x_2 - \left|\overrightarrow{MA_2}\right| \cdot \cos\gamma_{\overrightarrow{MA2}}} \right| \tag{17}$$

We can conclude as follows:

$$x_2 = \left|\overrightarrow{MA_2}\right| \cdot \sin\gamma_{\overrightarrow{MA2}} / \tan(\alpha + \gamma) + \left|\overrightarrow{MA_2}\right| \cdot \cos\gamma_{\overrightarrow{MA2}} \tag{18}$$

Then, the powder transport vector is determined. In addition, the transport length of the central particles is changed to

$$L_{AO}^{\alpha} = \left|\overrightarrow{A_2N}\right| \tag{19}$$

The outflow position vector $\overrightarrow{OA_2}$ is expressed as

$$\overrightarrow{OA_2} = \overrightarrow{OA_1} + \overrightarrow{A_1A_2} = \overrightarrow{OA_1} + \overrightarrow{A_1M} + \overrightarrow{MA_2} = \left[-W - (L + \chi)/\tan\gamma - \left|\overrightarrow{MA_2}\right| \cdot \cos\gamma_{\overrightarrow{MA2}}\right] \cdot i + \left|\overrightarrow{MA_2}\right| \cdot \sin\gamma_{\overrightarrow{MA2}} \cdot j \tag{20}$$

The injection offset vector $\overrightarrow{ON}$ can be given by Eq. (21), where x_1, x_2 are calculated in Eqs. (6, 18).

$$\overrightarrow{ON} = \overrightarrow{OM} + \overrightarrow{MN} = (x_1 - x_2) \cdot i \tag{21}$$

2.2.3 Adjustment of molten pool width

The boundary condition of powders falling into the pool is only changed with the adjustment (δ) of the molten pool width, by which the particle concentration distribution is not affected. As depicted in Fig. 2(c), the boundary after $-\delta$ adjustment is determined by Eq. (22).

$$\begin{cases} x(P_3) = (D - \delta)/2 \\ x(P_4) = -(D - \delta)/2 \end{cases} \tag{22}$$

2.3 Calculation of powder transport ratio

As confirmed, the powder flux actually tends to be of a Gaussian distribution [8], and the key position information are brought into the original Gaussian model merely to calculate powder transport ratio. Information of each key position and vector parameter after adjustments is listed in Table 1.

2.3.1 Particle concentration distribution

Figure 1 reflects the state of the powder flow field before adjustment of the powder injection parameter. It can be intercepted as discrete spaces with a height of dz_1 by multiple planes perpendicular to the Z_1 axis; thus, mass of powder particles stored in each space of dz_1 length in Z_1 direction is given by

$$m(z_1) = V_m \cdot t_{dz_1} = V_m \cdot \frac{dz_1}{V_{PE}} \tag{23}$$

where V_{PE} is derived from the kinematic equation of the central particle in powder flux and confirmed [13] as follows

$$V_{PE} = \sqrt{V_t^2 + (V_{P0}\cos\theta)^2} = \sqrt{V_{P0}^2 + 2g(L_{AO} - z_1)\sin\gamma} \tag{24}$$

Particle mass distribution of powder flux per unit length in z_1 direction is

$$C_G(z_1) = \frac{m(z_1)}{dz_1} = \frac{V_m}{V_{PE}} \tag{25}$$

Within any above cross-section of Gaussian flow field, powder particles are normally distributed (Fig. 1). Concentration distribution in the S_1 coordinate can be

$$C_G(x_1, z_1) = C_G(z_1) \cdot f_G(x_1; \mu, \sigma) = \frac{V_m}{\sqrt{V_{P0}^2 + 2g(L_{AO} - z_1)\sin\gamma}} \cdot \frac{1}{\sigma\sqrt{2\pi}} \exp\left[-\frac{(x_1 - \mu)^2}{2\sigma^2}\right] \tag{26}$$

After parameter adjustments in this paper, the concentration distribution in coordinate S_N (Fig. 3(b)), which is determined by the powder transport vector $\overrightarrow{A_2N}$, can be given by substituting information (Table 1) of step 2 into Eq. (26), such as transport distance (L_{AO}^{α}) and inclination (γ_2) for central particles. Using the coordinate offset vector in step 3 (Table 1) and the formula of coordinate translation Eq. (27), the concentration distribution in the original coordinate S_1 system is obtained. Coordinate offset vector $\overrightarrow{ON}$ is used to compute the location of the distribution maximum. In case of coordinate translation from S_N to S, then

$$\begin{cases} x_\alpha = x - \overrightarrow{ON} \\ z_\alpha = z \end{cases} \tag{27}$$

Table 1 Information of key positions and vectors

	Initial state	→Defocusing distance $+\chi$	→Powder feeding angle $+\alpha$	Step
Outflow position	A	A_1	A_2	——
Outflow position vector	$\overrightarrow{OA}$	$\overrightarrow{OA_1}$	$\overrightarrow{OA_2}$	1st for boundaries of powder flow
Position in X-direction	$-W$	$-W$	$x(\overrightarrow{OA_2})$, Eq.20	
Position in Z-direction	L	$L+\chi$	$z(\overrightarrow{OA_2})$, Eq.20	
Nozzle inclination	θ	θ	$\theta+\alpha$	
Divergence angle	φ	φ	φ	
Injection position	O	M	N	——
Powder transport vector	$\overrightarrow{AO}$	$\overrightarrow{A_1M}$	$\overrightarrow{A_2N}$	2nd for concentration distribution in injection position coordinates
Coordinate system	jOi	$j_M Mi_M$ [Fig.3(a)]	$j_N Ni_N$ [Fig.3(b)]	
Transport distance	L_{AO}	L_{AO}^{χ}	L_{AO}^{α}, Eq.19	
Transport inclination	γ	γ_1	γ_2, Eq.8	
Injection offset vector	——	$\overrightarrow{OM}$	$\overrightarrow{ON}$	3rd for coordinate system offset
	Initial state	→Pool width $-\delta$		4th for molten pool boundaries
$x(P_3)$	$D/2$	$(D-\delta)/2$, Eq.22		
$x(P_4)$	$-D/2$	$-(D-\delta)/2$, Eq.22		

After adjustments, the concentration distribution of the powder flow field can be concluded as follows:

$$C_G^{\alpha}(x_1,z_1)=\frac{V_m}{\sqrt{V_{P0}^2+2g\left(L_{AO}^{\alpha}-z_1\right)\sin\gamma_2}}\cdot\frac{1}{\sigma\sqrt{2\pi}}\exp\left[-\frac{\left(x_1-\overline{ON}-\mu\right)^2}{2\sigma^2}\right] \tag{28}$$

2.3.2 Boundary conditions of powder flow field

The boundary conditions are calculated by substituting the information (Table 1) of 1st and 4th step into the original Gaussian powder transport model. As the relative position of the powder flux and molten pool boundaries changes, ξ^{G}_{PT} expression by Eqs. (13–15) in [8] is no longer applicable. It can be determined by the positional relationship of P_1, P_2, P_3, P_4 (Figs. 1 and 2) and expressed as follows:

$$\xi_{PT}^{G}=\begin{cases}\int_{x(Q_4)}^{x(Q_3)}C_G^{\alpha}\cdot dL/\int_{x(Q_2)}^{x(Q_1)}C_G^{\alpha}\cdot dL & x(P_1)\geq x(P_3)\ \text{and}\ x(P_2)\leq x(P_4)\\ \int_{x(Q_2)}^{x(Q_3)}C_G^{\alpha}\cdot dL/\int_{x(Q_2)}^{x(Q_1)}C_G^{\alpha}\cdot dL & x(P_4)<x(P_2)<x(P_3)\ \text{and}\ x(P_1)>x(P_3)\\ \int_{x(Q_4)}^{x(Q_1)}C_G^{\alpha}\cdot dL/\int_{x(Q_2)}^{x(Q_1)}C_G^{\alpha}\cdot dL & x(P_2)<x(P_4)\ \text{and}\ x(P_4)<x(P_1)<x(P_3)\\ 1 & x(P_2)>x(P_4)\ \text{and}\ x(P_1)<x(P_3)\\ 0 & x(P_1)<x(P_4)\ \text{or}\ x(P_2)>x(P_3)\end{cases} \tag{29}$$

where $x(P_{i=1,2,3,4})$ and $x(Q_{i=1,2,3,4})$ are confirmed by Eqs. (4–7) in [13] and Eqs. (6–9) in [8] respectively, in which some initial condition variables should be updated according to the information in Table 1, such as

Table 2 Values of three adjusted parameters

Adjustable parameters	Symbol	No. of level	Level
Defocusing distance	χ (mm)	13	− 6/− 5/− 4/− 3/− 2/− 1/0/1/2/3/4/5/6
Powder feeding angle	α (°)	13	− 3/− 2.5/− 2/− 1.5/− 1/− 0.5/0/0.5/1/1.5/2/2.5/3
Pool width	δ (mm)	5	− 1/− 0.5/0/0.5/1

coordinate of outflow position A_2 [$x(\overrightarrow{OA_2})$, $z(\overrightarrow{OA_2})$], nozzle inclination (θ+α), and molten pool width (D−δ). As it mainly depends on the shape of powder nozzle, carrier gas flow rate, powder particle size, etc., the powder flux divergence angle (φ) in Fig. 1 remains unchanged in this paper approximately, which is the key parameter to calculate above boundary conditions.

2.4 Powder transport ratios under different adjustment amount

In order to observe the variation of ξ_{PT} with the parameters in a multi-dimensional space sufficiently, the adjusted parameter combination with three factors 13 × 13 × 5 levels is designed in Table 2. The mathematical model deduced in this article is compiled into the M-language program, which can be run in the MATLAB software. Other initial conditions substituted into the model are consistent with [8]. Using for-end loop command, 845 values of ξ_{PT} are calculated successively by the substitution of each level in Table 2.

3 Experimental procedure

The essence of the above model was to discuss the variation of powder flux concentration distribution (Eq. 28) and powder transport ratio (Eq. 29) after adjustments of the defocusing distance, powder feeding angle, and molten pool width. In order to verify the theoretical model, experiments were designed and carried out in two aspects.

3.1 Verification of the spatial distribution of powder flux

The spatial distribution of powder particles from the lateral nozzle in the experiment was close to Gaussian, which had been verified [8]. According to the modeling approach, the experimental verification for the particle concentration distribution after injection parameters adjustment was mainly from the perspective of key point coordinate information, such as outflow position (A, A_1, A_2), injection position (O, M, N), and boundary of powder flux (P_1, P_2), which would be measured by a coordinate measuring machine (CMM). This entire experimental process is shown in Fig. 4(a), and the scheme is listed in Table 3. Since the CMM has an independent measuring platform, a set of experimental devices was designed to approximate the powder feeding in real laser cladding process. The defocusing distance was controlled by a height-adjusting knob and vernier caliper, and the powder feeding angle was controlled by an angle-adjusting knob and inclinometer, which could be magnetically attracted to the powder feeding tube. After each powder feeding condition parameter was determined, powders sprayed from the nozzle were projected onto the surface of an A4 sheet of paper with glue, and then fixed by a transparent PVC plate. Each key point position could be measured by CMM after marking. The experimental scheme was designed to first raise the defocusing distance of the lateral powder feeder from the initial position by 4 mm, and then rotate the feeding nozzle by 3° clockwise. A total of three groups of measurements were developed, and the data of 12 measurement points are listed in Table 3.

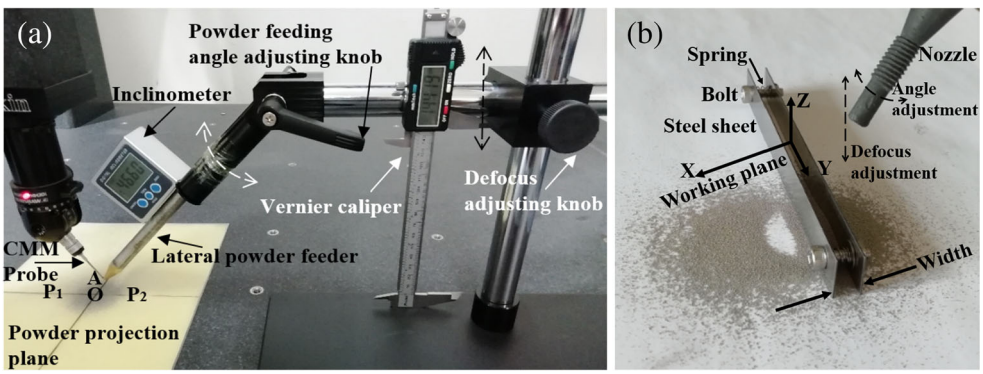

Fig. 4 Experimental verification for (a) powder flux distribution and (b) powder transport ratio

Table 3 Coordinate information of key points in powder flux

	Initial state				→Defocusing distance $+\chi$ ($\chi = 4$ mm)				→Powder feeding angle $+\alpha$ ($\alpha = 3^{\circ}$)			
	A	P_2	P_1	O	A_1	P_2	P_1	M	A_2	P_2	P_1	N
Experimental data	(− 5.2, 8.9)	− 2.11	2.0	− 0.1	(− 5.2, 12.9)	− 1.5	4.0	1.3	(− 9.9, 10.3)	− 7.1	− 2.3	− 4.7
Theoretical data	(− 5.2, 8.9)	− 2.0	2.0	0.0	(− 5.2, 12.9)	− 1.0	3.9	1.5	(− 9.9, 10.3)	− 6.7	− 2.4	− 4.6
	Figure 5(a)				Figure 5(b)				Figure 5(c)			

A, A_1, A_2—outflow position, P_2—left boundary of powder flow, P_1—right boundary of powder flow, O, M. N—injection position

3.2 Verification of the powder transport ratio

In Fig. 4(b), a powder collection device equipped with two steel sheets, springs, and hexagon socket bolts was used to verify the powder transport ratio under different powder injection parameters. All tests were programmed with 2.322 g/min powder feed rate during 10 s and the placement was marked to ensure that each test has the same initial state before parameter adjustment. As the influence of molten pool width had been developed and compared with theoretical values in Fig. 7 of [8], powder transport ratio had been measured only after adjusting the defocusing distance and powder feeding angle respectively, which ranged from − 2 to 10 mm by 2 mm increments for χ, and from − 3° to 3° by 0.5°increments for α.

By weighing the powder quantity stored between above two steel sheets always set at 3 mm distance, the experimental data could be estimated and distributed in Fig. 6.

4 Results and discussion

4.1 Experimental verification for the model

Similar to the experiment in Section 3.1 before, adjustment of defocusing distance χ (+ 4 mm) and powder feeding angle α (+ 3°) was substituted into the theoretical model successively. In Fig. 5(a–c), the concentration distribution of powder particles calculated by Eq. 29 is projected into a two-dimensional

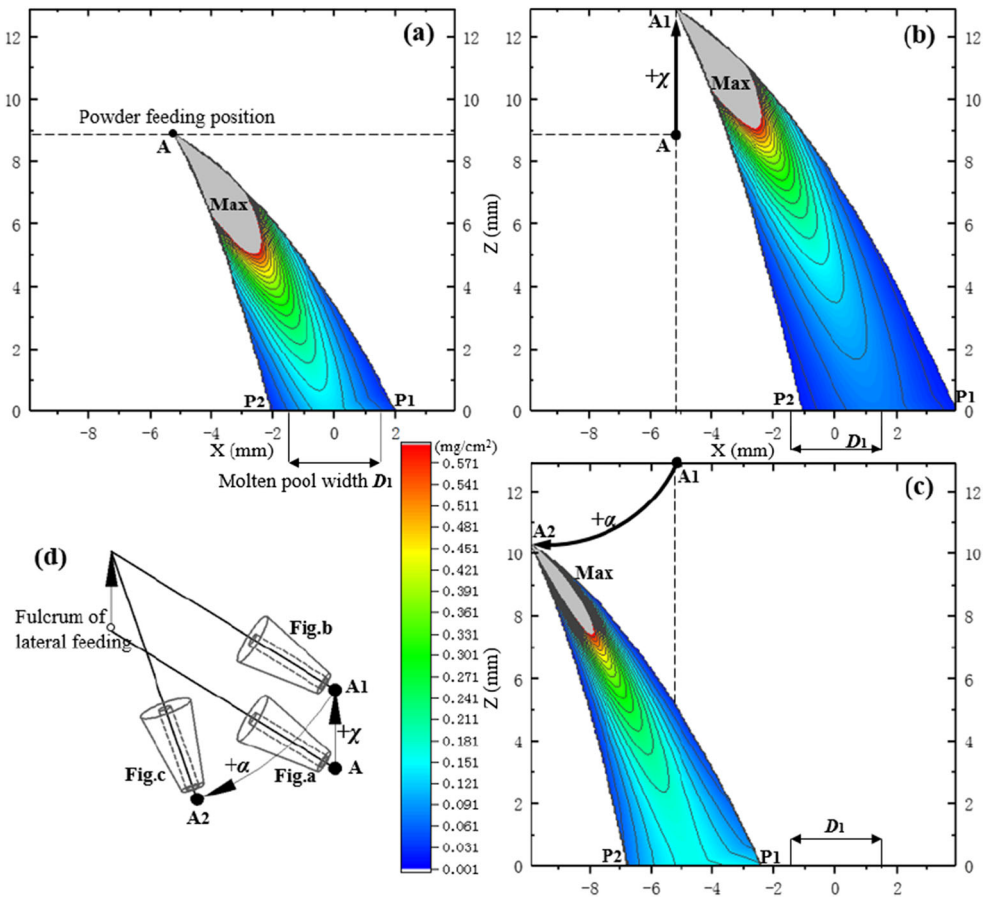

Fig. 5 Particle concentration distribution of powder flux. (a) Initial state. (b) Adjustment of defocusing distance. (c) Adjustment of powder feeding angle. (d) Relationship of nozzle position

space of 13.8 × 12.9 mm^2 (− 9.9 mm ≤ X ≤ 3.9 mm, 0 ≤ Z ≤ 12.9 mm), which can be illustrated in Fig. 5(d). According to the cloud scale, the powder flux conforms to a Gaussian distribution and its key point coordinates are extracted in Table 3 for comparison with the experimental measurements. As the model is solved analytically, the calculation of the outflow position (A, A_1, A_2) is accurate, while small deviations for the injection position (O, M, N) and boundary of powder flow (P_1, P_2) exist probably due to inaccurate substitution of initial conditions, such as γ and φ. Despite some errors, the results show that this model can truly reflect the distribution and spatial position of the powder flux after adjusting the powder injection parameters. The change of the powder flux position relative to the fixed molten pool causes a different ξ_{PT}, which is discussed further.

Moreover, in the theoretical calculation process, the powder feeding rate V_m is set as 2.322 g/min, which was measured from the actual lateral powder feeding nozzle in laboratory. In a three-dimensional space, the real powder stream can be intercepted by multiple planes parallel to the XOZ direction (Fig. 1), and then, slice photos containing particle distribution information are stacked, which can be regarded as the particle concentration distribution in the two-dimensional space shown in Fig. 5. The shape of the molten pool can also be projected on the XOZ plane to obtain the molten pool width. Finally, the powder efficiency can be estimated by mass ratio of powder particles falling within this width range to all powders injected from the nozzle. In essence, it is a dimension reduction operation from 3D to 2D.

For the experiment as described in Section 3.2, the one-dimensional variation of ξ_{PT} with χ or α is calculated by Eq. 29 and plotted in Fig. 6, in which the experimental data under 3 mm molten pool width condition was also distributed. The relative height of the lateral nozzle to the cladding plane is 8.9 mm in the initial state of this model, which is determined by the experimental conditions. Therefore, it is meaningless to reduce the defocusing distance (χ) too much in the experiment because of the physical interference between the nozzle and cladding parts. Experiments for χ less than − 2 mm were not carried out in Fig. 6(a). It is set as initial state ($\chi = 0$, $\alpha = 0$) that the central particle of powder flux just falls in the middle of molten pool, so any adjustment of defocusing distance and powder feeding angle would lead to a decrease of ξ_{PT}. Moreover, results for positive (χ, $\alpha \rightarrow +$) and negative (χ, $\alpha \rightarrow -$) adjustment of the lateral powder feeding parameter have asymmetry, in which the latter corresponds to a lower ξ_{PT} under the same adjustment value. That is, reducing the defocusing distance or inclination angle of the lateral nozzle will greatly affect the amount of powder particles fed into the molten pool. This can be both observed from theoretical and experimental results, which means this established model can describe the influence of powder feeding parameters on real powder efficiency.

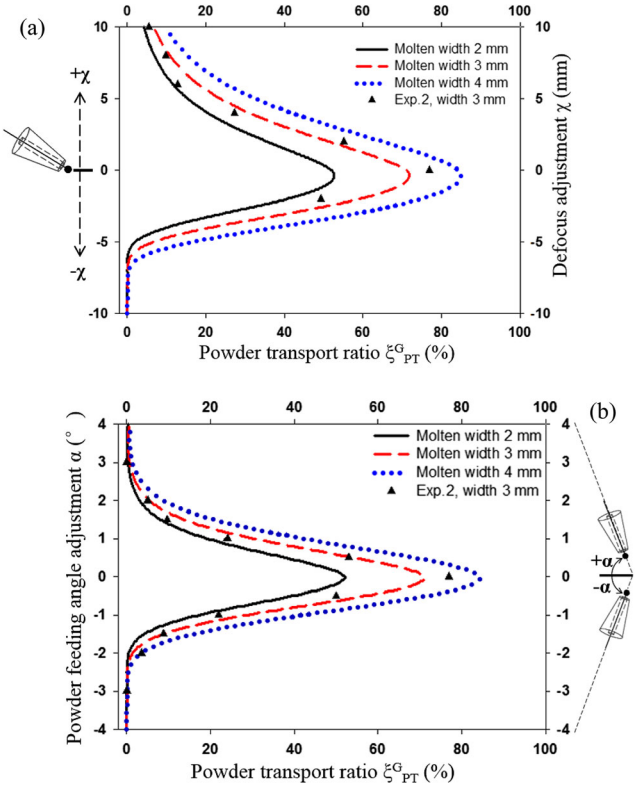

Fig. 6 Variation of powder transport ratio with (a) defocusing distance and (b) powder feeding angle

4.2 Influence of powder feeding parameters

According to Section 2.4, ξ_{PT} values corresponding to 13 × 13 × 5 levels of three variables (χ, α, δ) were calculated. These three-dimensional point clouds are displayed in the form of some oriented two-dimensional cloud images to reflect the influence of the powder feeding parameters on ξ_{PT}, which is also illustrated in Fig. 7 for their orientation relationships.

As shown in Fig. 7(b, c), ξ_{PT} increases with increasing molten pool width under any conditions, and the maximum value of this increment, which is related to the defocusing distance or powder feeding angle, occurs near the initial position without change of χ or α. As mentioned before, the positive and negative adjustments for the above parameters are asymmetrical. In Fig. 7(a), ξ_{PT} value can be maintained at a higher (/stable) level by simultaneous adjustments of χ and α in negative (/positive) direction, but a lower level as ($\chi > 0$, $\alpha < 0$) or ($\chi < 0$, $\alpha > 0$). For the physical model, as the lateral nozzle is located at the position where central particles can fall into the molten pool center, the powder efficiency increases significantly (/slightly) with the reduction (/increase) of defocusing distance and powder feeding angle simultaneously. From the above analysis, a qualitative judgment on the variation trend of ξ_{PT} can be made by the direction

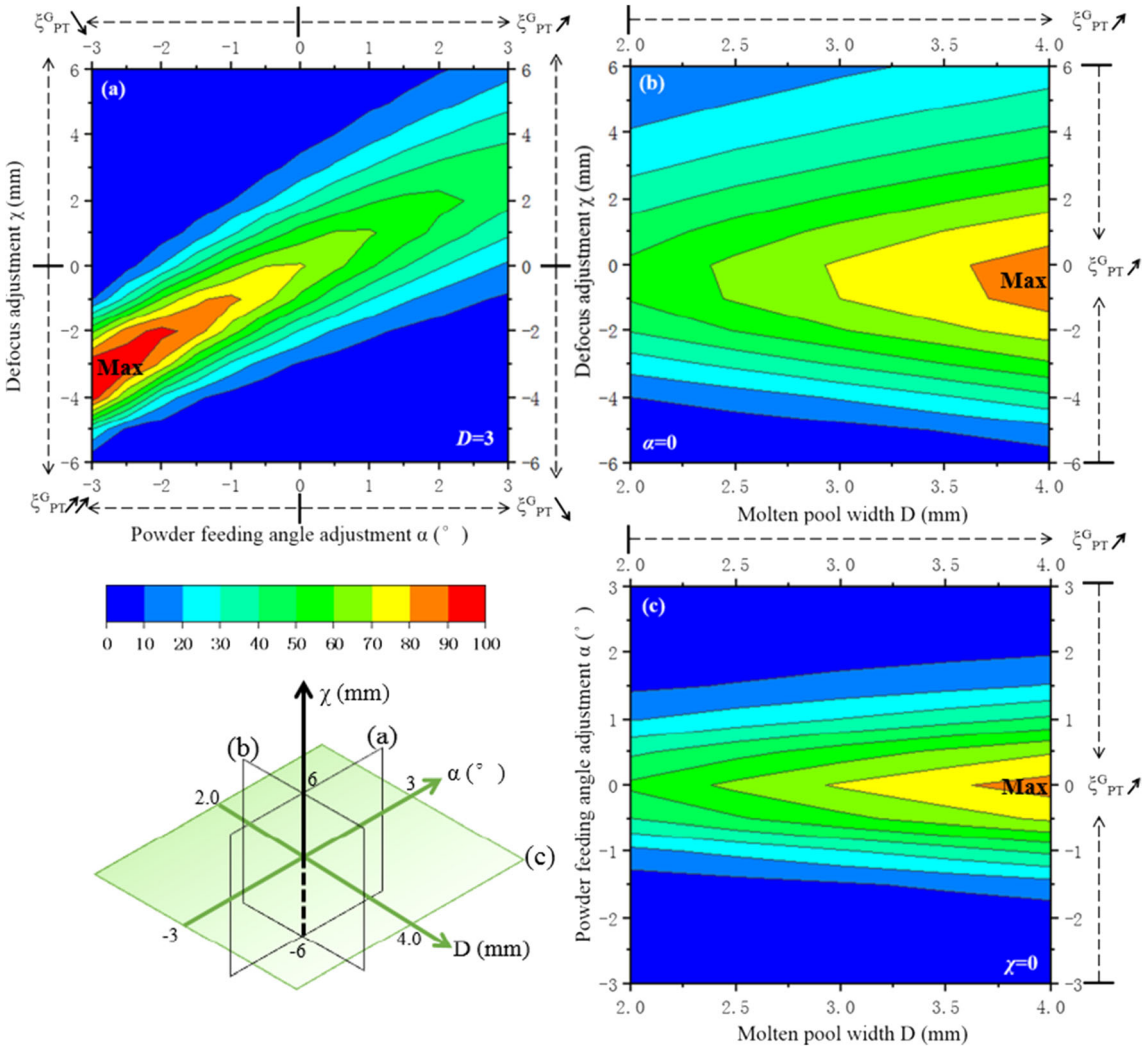

Fig. 7 Cloud images of powder transport ratio in (a) χ-α, (b) χ-D, and (c) α-D coordinate system

(+, −) of the adjusted parameters (χ, α, δ) preliminarily. The significance of this model is that ξ_{PT} can be predicted quantitatively under any combination of the above parameters.

4.3 Process window

As shown in Fig. 8, the process window can be drawn by overlapping contours with ξ_{PT} values of 60% in the same coordinate system (χ-α), which corresponds to different molten pool widths ($\delta = -0.5/0/0.5/1$ mm). In addition, the contour line of 99% ξ_{PT} with 4 mm molten pool width is also displayed. According to the gradient direction from 60 to 99%, regional coordinates (χ, α) within contours (δ) can be regarded as a combination of adjusted parameters with ξ_{PT} greater than 60%. In addition, the adjustable range of χ and α increases with the width of the molten pool ($\delta\nearrow$). Moreover, the process window is intentionally divided into two regions ($\chi < 0$ and $\chi > 0$). Although a higher

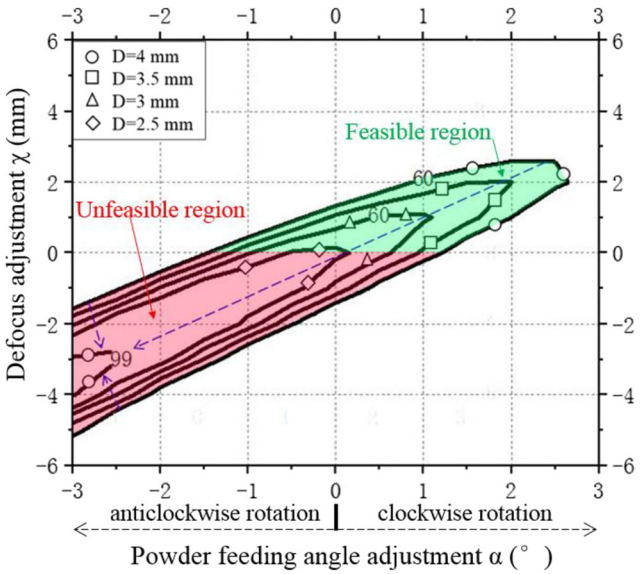

Fig. 8 Process window with powder transport ratio larger than 60%

ξ_{PT} is obtained in the former ($\chi < 0$), interference would be caused by reducing the defocusing distance as the lateral nozzle is close to the cladding substrate. Thus, more feasible adjusted parameters should be selected in the green region ($\chi > 0$) of the window.

5 Conclusion

Based on the established powder transport model for laser cladding by lateral powder feeding, the function expression of the powder transport ratio is derived by a vector geometry relation, in which the adjusting parameters of defocusing distance, powder feeding angle, and molten pool width are set as input variables and substituted into the model in turn. The distribution of powder flux and powder transport ratio after adjustment of the above parameters have been verified by experiments and results are basically in agreement with theoretical values. Then, values of three variables corresponding to $13 \times 13 \times 5$ levels are calculated by MATLAB software to reflect the effect of the injection parameters on the powder transport ratio. Some conclusions can be summarized as follows.

- The powder transport ratio increases with the width of the molten pool, and this increment is affected by the defocusing distance or powder feeding angle.
- As the central particles of the powder flux fall into the molten pool center, the powder transport ratio is reduced by a single parameter adjustment of the defocusing distance or powder feeding angle, which is asymmetrical for positive or negative direction.
- As central particles fall into the molten pool center, the trend for the powder transport ratio by simultaneous adjustments of the defocusing distance and powder feeding angle would be judged by a vector product of these two parameters. A positive vector product corresponds to a high level of the powder transport ratio, which increases with the adjustment.
- For an arbitrary combination of three injection parameters, the powder transport ratio can be calculated by this model. Furthermore, the process window can be drawn, and the above parameter combinations corresponding to a powder transport ratio larger than 60% are determined in this paper.

Funding information This study was financially supported by the Basic Scientific Research Service Fee of Central University (No. 3142015012, No. 3142015097) and Hebei Key Laboratory of Safety Monitoring of Mining Equipment.

References

1. Tian X, Sun B, Heinrich J, Li D (2013) Scan pattern, stress and mechanical strength of laser directly sintered ceramics. Int J Adv Manuf Technol 64(1–4):239–246. https://doi.org/10.1007/s00170-012-3994-6
2. Fu Y, Loredo A, Martin B, Vannes AB (2002) A theoretical model for laser and powder particles interaction during laser cladding. J Mater Process Technol 128(1–3):106–112. https://doi.org/10.1016/S0924-0136(02)00433-8
3. Kumar A, Paul CP, Pathak AK, Bhargava P, Kukreja LM (2012) A finer modeling approach for numerically predicting single track geometry in two dimensions during laser rapid manufacturing. Opt Laser Technol 44(3):555–565. https://doi.org/10.1016/j.optlastec.2011.08.026
4. Lalas C, Tsirbas K, Salonitis K, Chryssolouris G (2007) An analytical model of the laser clad geometry. Int J Adv Manuf Technol 32(1–2):34–41. https://doi.org/10.1007/s00170-005-0318-0
5. Yang N, Yang X (2008) Powder flow field distribution with different parameters in coaxial laser cladding. Proceedings of the SPIE: Lasers in Material Processing and Manufacturing III 6825:24. https://doi.org/10.1117/12.765634
6. Li Y, Yang H, Lin X, Huang W, Li J, Zhou Y (2003) The influences of processing parameters on forming characterizations during laser rapid forming. Mater Sci & Eng: A 360(1–2):18–25. https://doi.org/10.1016/S0921-5093(03)00435-0
7. Goodarzi DM, Pekkarinen J, Salminen A (2017) Analysis of laser cladding process parameter influence on the clad bead geometry. Weld World 61(5):883–891. https://doi.org/10.1007/s40194-017-0495-0
8. Gong XY, Wang JH, Feng HM (2019) Lateral powder transport model with Gaussian distribution in laser cladding. Int J Adv Manuf Technol 102(9–12):3747–3756. https://doi.org/10.1007/s00170-019-03499-3
9. Lin J (1999) A simple model of powder catchment in coaxial laser cladding. Opt Laser Technol 31(3):233–238. https://doi.org/10.1016/S0030-3992(99)00046-8
10. Pinkerton AJ, Li L (2004) The significance of deposition point standoff variations in multiple-layer coaxial laser cladding (coaxial cladding standoff effects). Int J Mach Tools & Manufacture 44(6):573–584. https://doi.org/10.1016/j.ijmachtools.2004.01.001
11. Liu J, Li L (2007) Effects of process variables on laser direct formation of thin wall. Opt Laser Technol 39(2):231–236. https://doi.org/10.1016/j.optlastec.2005.08.012
12. Liu J, Li L (2005) Study on cross-section clad profile in coaxial single-pass cladding with a low-power laser. Opt Laser Technol 37(6):478–482. https://doi.org/10.1016/j.optlastec.2004.07.010
13. Gong XY, Zhang YZ, Liu MK (2013) Powder transport model for laser cladding by lateral powder feeding: I. powder flow field with cylindrical distribution. Int J Adv Manuf Technol 67(9–12):2501–2509. https://doi.org/10.1007/s00170-012-4667-1